Anal Bioanal Chem (2007) 387:649–661
DOI 10.1007/s00216-006-0907-2

ORIGINAL PAPER

Early oriented isothermal crystallization of polyethylene studied by high-time-resolution SAXS/WAXS

**N. Stribeck · A. Almendarez Camarillo · U. Nöchel ·
P. Bösecke · R. K. Bayer**

Received: 5 April 2006 / Revised: 2 October 2006 / Accepted: 6 October 2006 / Published online: 7 November 2006

Abstract During cooling from the quiescent melt of a highly oriented polyethylene rod, highly oriented proto-lamellae are formed first, which are not crystalline. This is shown in scattering data which are recorded on two-dimensional detectors with a cycle time of 1 s and an exposure of 0.1 s. In the experiments small-angle X-ray scattering (SAXS) and wide-angle X-ray scattering (WAXS) are registered simultaneously during the first 3 min after quenching to a crystallization temperature. A non-uniform thickness between 20 and 100 nm is characteristic for the ensemble of proto-lamellae. During the first minute of isothermal treatment the number of proto-lamellae slowly increases without a change of the thickness distribution. As crystallization starts, the crystallites are not oriented in contrast to the proto-lamellae. During crystallization the layer thickness distribution narrows. The number of lamellae rapidly increases during the following 2 min of isothermal treatment (at 128 °C and 124 °C). The results are obtained by interpretation of the WAXS and of the multidimensional chord distribution function (CDF), a model-free real-space visualization of the nanostructure information contained in the SAXS data.

Keywords SAXS · Polyethylene · Crystallization

Introduction

Structure evolution during crystallization of polymer materials has been studied for several decades. Since industry has returned to the tailoring of bulk polymer materials, this field is back in the focus of scientific interest [1–13]. Nevertheless, the views concerning the mechanisms of nanostructure evolution are still conflicting, because the experimental data collected so far are still insufficient.

Structure evolution can be monitored in situ by means of X-ray scattering. On the other hand, the recorded data require model fitting or mathematical evaluation if simplified notions are not applied. The situation is aggravated by the fact that most of the investigations of structure evolution in polymers are still carried out on isotropic samples: the information content of the corresponding scattering curve is so low that simplistic models (e.g., the ideal lamellar system, spinodal decomposition, nucleation-and-growth) have to be employed. Several predictions of such models are only significant if they are tested against data of ideal polymers with vanishing polydispersity. As a result, the focus of research concerning structure evolution has turned away from the study of applied polymer materials.

Compared to the scattering curve of an isotropic sample, the information content of an anisotropic scattering pattern is clearly higher. Thus the significance of the results from structure evolution studies can be considerably enhanced

---

Dedicated to Prof. Dr. F. J. Baltá Calleja on the occasion of his 70th birthday.

N. Stribeck (✉) · A. Almendarez Camarillo · U. Nöchel
Institute of Technical and Macromolecular Chemistry,
University of Hamburg,
Bundesstr. 45,
20146 Hamburg, Germany
e-mail: Norbert.Stribeck@desy.de

P. Bösecke
ESRF,
6 rue Jules Horowitz, B.P. 220,
38043 Grenoble Cedex 9, France

R. K. Bayer
Institut für Werkstofftechnik, Universität GH Kassel,
34109 Kassel, Germany

without the need to resort to simplified notions if anisotropic samples are studied and properly evaluated. Our contribution in this field is based on the development of automatic data evaluation methods for the small-angle X-ray scattering (SAXS) of oriented materials with fiber symmetry, aiming at the model-free visualization of nanostructure and its evolution processes [14–18]. The chance to apply such a method to the investigation of polymer crystallization arose when we found that the orientation memory of a highly oriented material can be preserved in the melt. Consequently, a subsequent crystallization results in a semicrystalline structure that is highly oriented at least during a certain period of the experiment [19]. Such preparation of an oriented melt can be carried out for many polymer materials, and we decided to pick commercial polymer grades for our crystallization studies in order to collect information on their nanostructure evolution mechanisms.

In contrast to results obtained by studying series of macromolecular compounds specially designed by sophisticated chemistry, our method can directly be applied to materials that are technically used. On the other hand, the newly introduced reconstruction procedures are not yet as well-engineered as, e.g., in the field of medical application of tomography, where software engineering is an important research activity.

As today we combine the use of well-equipped synchrotron radiation facilities with an advanced concept of analytics for the investigation of oriented polymer materials, it becomes possible to study processes of structure transfer in two or three dimensions of physical space without the need to resort to models. Recently we reported results on the nanostructure evolution mechanisms studied during melting and crystallization of injection-molded highly oriented polyethylene (Lupolen 6021D) [19–23] with cycle times of 30 s and 7 s. Here we study a very similar sample but focus on the initial 3 min of isothermal crystallization scanned with a high time-resolution (cycle time of 1 s). Similar to considerations of Baltá [12, 24] and other researchers, our main goals are the identification of structure evolution before the onset of crystallization, the separation of significant from insignificant features in our data, and the understanding of the coupling between the emerging nanostructure and crystallite formation.

Experimental

Overview

Highly oriented polyethylene (PE) rods of 6-mm diameter are prepared by high-pressure injection molding (HPIM) [19, 25] from commercial material. The highly oriented material is molten in a heat stage at 139 °C for 3 min. It is then quenched to different crystallization temperatures. Two-dimensional (2D) small-angle X-ray scattering (SAXS) and wide-angle X-ray scattering (WAXS) are simultaneously recorded during the first 195 s after quenching of the sample with a cycle time of 1 s at beamline ID02, ESRF, France.

Material

We start from commercial high-density, low-branched Ziegler-Natta-type polyethylene (PE) (Lupolen 6021 D, BASF, M_w=182,000 g/mol, M_n=25,000 g/mol, density 0.962 g/cm^3, melt flow index 0.2). Rods (6-mm diameter, 10-cm length) are prepared using the HPIM [19, 25] process to obtain a material with high preferential orientation. An equilibrated, low-temperature melt (150 °C) is injected under high pressure into a cold mold. Maximum mold pressure is 400 MPa and final mold pressure 350 MPa after 180 s. The material exhibits bimodal melting in differential scanning calorimetry (DSC) with peak maxima at 131 °C and 141 °C.

Scattering experiments

The experiments are performed at the synchrotron beamline ID02 [26] of ESRF. Unlike in a previous study [22, 23], the primary beam is not attenuated here. Instead, the exposure time is reduced to 0.1 s. The wavelength of the X-ray beam is 0.1 nm. SAXS patterns are collected by a 2D position-sensitive XRII–FReLoN (“X-Ray Image Intensifier, Fast Readout, Low Noise”) CCD detector developed at ESRF (driven in 1,024×1,024 pixel mode, each of 0.164×0.164 mm^2, 14-bit resolution). The sample-to-detector distance is set to 10 m. The sensitive area on the detector covers a reciprocal space volume equivalent to $-0.09\ \mathrm{nm}^{-1} < s_{12}, s_3 < 0.09\ \mathrm{nm}^{-1}$ with the scattering vector **s** in cylindrical coordinates and the norm $s = \sqrt{s_{12}^2 + s_3^2} = (2/\lambda)\sin\theta$. 2θ is the scattering angle, and s_3 is in the direction of the fiber axis (meridian). Thus the outer edge of the active area of the detector corresponds to a minimum Bragg spacing of 1/(0.09 nm^{-1})=11 nm. A maximum Bragg spacing of 220 nm is resolved. Wide-angle X-ray scattering (WAXS) is simultaneously recorded using a MCP-Sensicam CCD detector [27, 28] placed at a short distance from the sample in an offset position. Thus the WAXS detector monitors a region around the equator of the scattering pattern. Samples sliced to 2 mm thickness are mounted in a Mettler-Toledo FP82HT hot stage and subjected to a temperature program in the synchrotron beam.

Data evaluation and CDF

Data are evaluated using programs self-written in *pv-wave* [29]. The sources are available for download [30]. During data evaluation all patterns are normalized with respect to the incident flux. Parasitic background is subtracted under consideration of the measured absorption factor. Blind areas on the detector resulting from the beam stop and its holder are masked. Each pattern is aligned and centered. As far as possible the blind areas are filled utilizing obvious symmetry considerations.

In order to visualize the domain structure in real space, the chord distribution function (CDF) analysis is utilized [16]. For the CDF analysis the 2D SAXS patterns are evaluated. In a first step the remnant central hole is filled by two-dimensional extrapolation utilizing radial basis functions [31]. As described in earlier work [16, 19, 23, 25, 32–37], the scattering intensity is projected onto the (s_1,s_3)-plane, multiplied by s^2, then regridded to 512×512 pixels. A 2D density fluctuation background is determined by spatial frequency filtering and subtracted, resulting in the interference function $G(s_{12},s_3)$. $G(s_{12},s_3)$ is subjected to 2D Fourier transformation yielding the 3D chord distribution function (CDF),

$$z(s_{12}, s_3) = F_2(-G(s_{12}, s_3)).$$

The results of the intermediate steps of the computation have been demonstrated in several papers [16, 32, 38].

The discussion of the CDF in terms of the nanodomain topology [16, 25, 33, 39] inside the sample is straightforward, since the CDF is defined [16] by the Laplacian of Vonk’s multidimensional correlation function [40]. As such it presents the autocorrelation of the surfaces of the (nanosize) domains in space in the same manner as Ruland’s interface distribution function (IDF) does [41, 42] for one-dimensional structures as a function of distance.

Experimental differences with respect to the previous study

We have used new samples here compared to previous experiments with low time-resolution [23]. The old PE rods are used up. With a newly designed mold for the injection-molding press we can produce many rods per hour instead of one rod per day, but the achievable maximum pressure is lower. Adjusted to 400 MPa (instead of 444 MPa) we obtain a material very close to the former one by molding from a cooler melt (150 °C instead of 160 °C). Similarity of the nanostructure is verified by SAXS and DSC tests. At the beamline we now rotate the sample by 90° so that the fiber axis is pointing in the horizontal direction. The reason is that the 2D WAXS detector can only monitor a quarter of the pattern, and by rotating the sample we now observe the equatorial region of the WAXS data where the strong reflections of oriented PE show their maxima.

Because of the short exposure required in high-time-resolution experiments it is no longer suitable to attenuate the primary beam (previously we used an attenuation factor 10). This time we encounter problems to keep the melt in the beam throughout the experiment. Either the viscosity of the molten sample is insufficient and the cooling air stream blows the sample out of the holder, or the material is not completely molten because the melt annealing temperature is too low. A solution is found by mounting the sample between two thin sheets (20 μm) of aluminum with only a little hole for the beam to pass through. With the sample now shielded we can use full-stream cooling air. Thus we receive a higher quenching rate. Finally, the formerly used melt annealing temperatures must be reduced by 2 °C in order not to erase the orientation memory of the melt. Many samples are consumed in this trial-and-error optimization and finally 2 samples are left over for the intended experiments. After these adjustments the structure evolution observed in earlier experiments [23] is well reproduced.

The time-resolution of the experiments presented here is finer by 1 order of magnitude compared to the earlier study [23]. On this time-scale it becomes questionable if the experiments can still be named “isothermal” in the full sense of its meaning, even if the cooling power is now higher than before. Here we discuss data from 2 crystallization experiments. At the high crystallization temperature (128 °C) the isothermal level is reached 52 s after the start of quenching from the melt annealing temperature of 139 °C. At the medium crystallization temperature (124 °C) it takes 64 s until the crystallization temperature is reached.

Results and discussion

Direct observations

Figure 1 displays consecutive scattering data from the crystallization experiment at the lower temperature (124 °C). Figure 1a presents the scattering data from our newly prepared HPIM rod material before heat treatment. The central part of the recorded SAXS pattern is presented in a 3D surface plot. The fiber axis (meridian) is indicated by a double-headed arrow. As in our previous studies [19, 22, 25] the new samples cut from the outer shell of the rod exhibit highly oriented SAXS comprising a point-shaped long-period peak at 122 nm, an intensity ridge extending along the meridian, and an equatorial streak. The recorded WAXS pattern is shown in a grayscale photographic-film representation. In order to display weak reflections sufficiently well we mimic overexposure at a clipping level of 70%. Only a section of the full pattern is covered, because the detector is mounted in an offset position to let the SAXS pass by. Because of detector tilt a geometric distortion has to be corrected and, finally, the valid scattering data are restricted to a wedge-shaped area. Distortion remains in a narrow, ring-shaped region on the very right of each image. In the WAXS

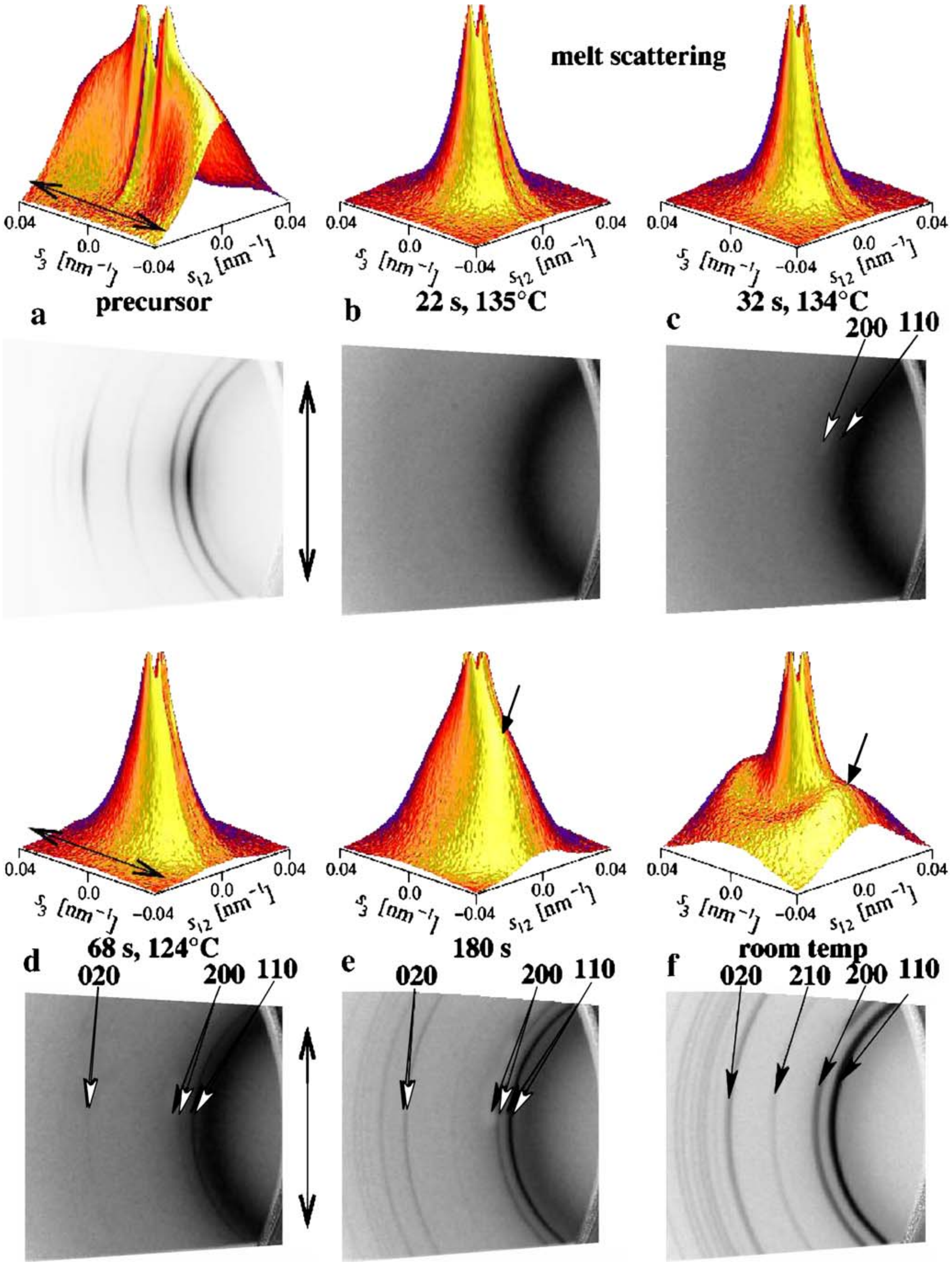
melt scattering
0.04
0.0
s_3 [nm^{-1}]
−0.04
0.0
s_{12} [nm^{-1}]
0.04
a
precursor
b
22 s, 135°C
c
32 s, 134°C
200
110
d
68 s, 124°C
e
180 s
f
room temp
020
210
200
110

◀ **Fig. 1** SAXS (*surface plots*) and WAXS (*grayscale*) during oriented isothermal crystallization of polyethylene. *Double-headed arrows* indicate fiber axis. Intensities on logarithmic scale with varying full scale value. **a** Injection-molded rod before processing. **b** 22 s after quenching from 139 °C to 124 °C: minimum SAXS, no WAXS. **c** 32 s after quenching. The main PE WAXS reflections appear isotropic. **d** 68 s after quenching. First increase of SAXS, more isotropic WAXS (*open arrow heads* high-temperature peak positions, *filled arrow heads* room-temperature peak positions). **e** 3 min after quenching. Strong discrete SAXS with fiber symmetry, strong isotropic WAXS. **f** Ultimate scattering at room temperature

of the original material we observe a superposition of highly oriented crystallites (intensity spots on the meridian) and almost isotropic ones (Debye-Scherrer rings).

Twenty two seconds after starting the quenching, WAXS of the melt (Fig. 1b) shows an amorphous halo only. The SAXS is so low that the reconstruction of missing data does not yet work perfectly: on the meridian an intensity decrease is observed where the holder of the primary beam stop was crossing the pattern. A structural feature of the observed scattering pattern of the melt indicates that the melting of this sample, indeed, is not perfect. The shape of the SAXS “melt scattering” appears elongated in the meridional direction. This feature is invisible during the experiment, but can be observed afterwards in a properly scaled logarithmic 3D plot. Later the CDF analysis will show (Fig. 6b in comparison to Fig. 5b) that this pattern is particle scattering of oriented proto-lamellae–lamellar domains with a higher density than the surrounding melt but no crystallinity. So the crystallites from the lamellae have been molten, whereas the density in the sample has not been equilibrated. We observe oriented nanostructure in a polyethylene melt.

After 32 s the temperature has dropped to 134.1 °C (Fig. 1c). The SAXS is still the same. Nevertheless, in the WAXS pattern faint reflections are first observed on Debye-Scherrer rings indicating that the orientation of the crystallites is isotropic or at least very low. It takes 68 s after quenching until a discernible shape-change of the SAXS intensity is observed in the 3D plot. At that time the temperature of the material has arrived at the crystallization level, and clear isotropic WAXS reflections are observed (Fig. 1d). The SAXS pattern, on the other hand, remains highly anisotropic and a long-period reflection is developing on the meridian (Fig. 1e). The WAXS is completely isotropic. It is noteworthy that the isotropy of only two vectors (e.g., 110 and 200 reflections) in the plane normal to the chain direction are sufficient to guarantee that every direction including the chain directions (e.g., imaginary 00ℓ reflections) are distributed at random. The orientation distribution of the chain directions would be uncertain only if *an*isotropy of the 110 and 200 reflections were observed. The reflection positions at high temperature (open arrow heads) are shifted towards smaller scattering angles with respect to their positions at room temperature (filled arrow heads) because of thermal expansion of the crystals.

Completely isotropic WAXS is observed at room temperature, whereas the SAXS shows a complex pattern which can be explained by the superposition of an isotropic and an anisotropic nanostructure (Fig. 1f).

In summary, the experiment shows that isotropic crystallites can grow in a melt which is highly anisotropic, nanostructured, and amorphous.

Figure 2 presents selected data from the isothermal crystallization experiment at high temperature (128 °C). Compared to the experiment presented first, here the SAXS of the melt looks isotropic even in a scaled-up logarithmic representation. The WAXS only shows an amorphous halo. It takes 65 s from quenching until the SAXS pattern starts to change its shape (Fig. 2a). A peak (arrow) with a long period of 110 nm is emerging at the meridian. The high-resolution SAXS setup is required to resolve this feature. In a common SAXS setup it is hidden behind the beam stop [38]. At this time the WAXS diagram still shows an amorphous halo only. After 85 s very faint indications of the strong PE reflections (110 and 200) are discovered. At 95 s the reflections are strong enough to recognize random orientation of the crystallites. After 135 s the 020 reflection can be detected. After 145 s (Fig. 2b) it is even indicated in a printed image. Again, the formation of crystallites is preceded by the formation of a highly oriented nanostructure of proto-lamellae. The observed long-period reflection shows that there is some faint correlation among some of these layers. Even in this experiment we do not observe preferential orientation of the crystallites during the first 3 min of isothermal crystallization.

Wang et al. [4] have postulated that such an observation of “SAXS before WAXS” may be caused from a systematic mismatch between a high sensitivity (for the identification of the beginning of crystallization) of the SAXS detector and a low sensitivity of the WAXS detector. They have corroborated their argument by analysis of simulated isotropic scattering data and concluded that crystalline fractions lower than 0.01 cannot be detected. On the other hand, Panine et al. [13] have experimentally shown that—at least for the instrument ID02—the WAXS detector is capable of resolving crystalline fractions well below 0.001. In our experiments the WAXS detector is never saturated but receives an optimum number of photons, the observed reflections are sharp and can be detected very early—in particular by visual inspection of the 2D scattering image.

The ultimate structure at room temperature (Fig. 2c) is very similar to the structure found after cooling from the lower crystallization temperature. For the studied material this independence of the ultimate structure from the history of the crystallization process has been found before in

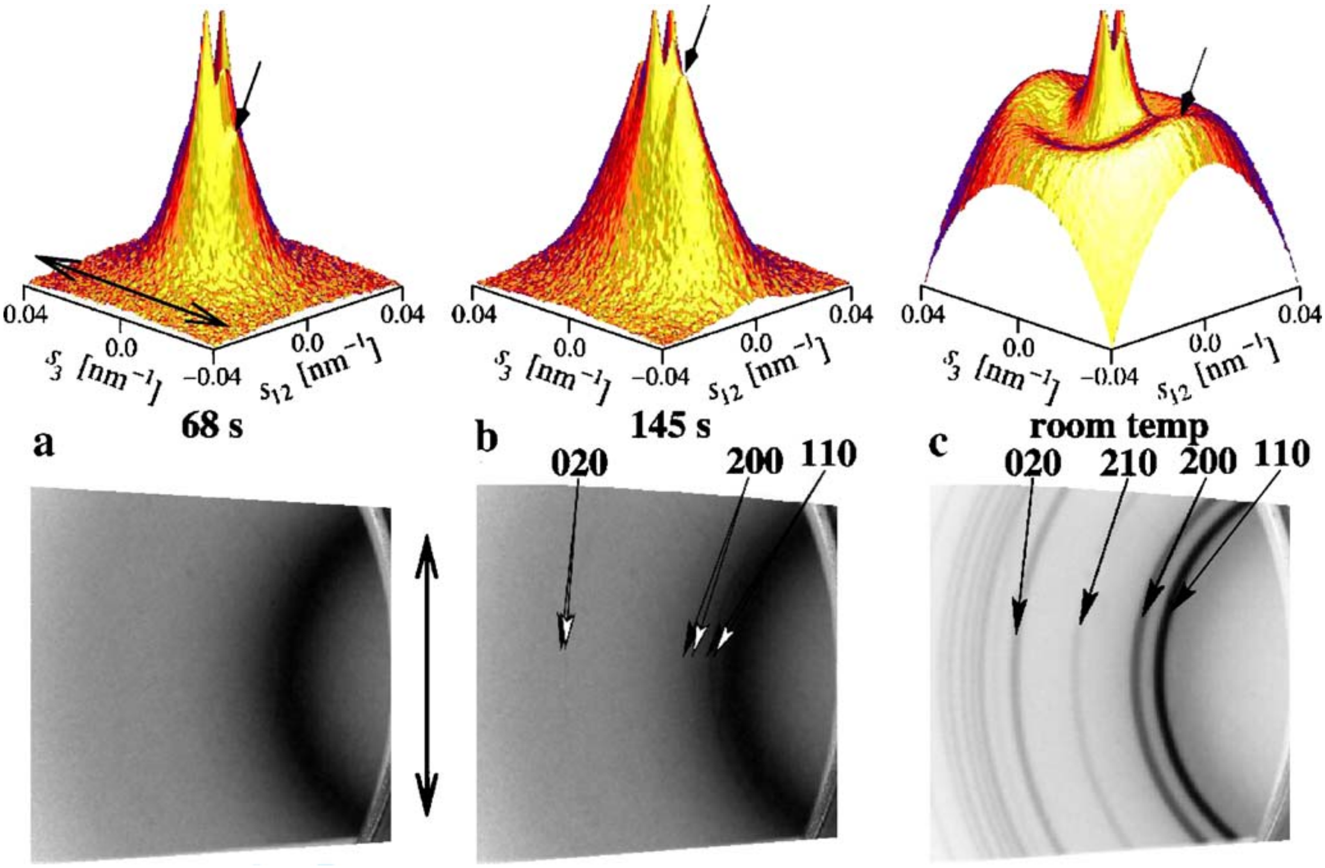

Fig. 2 An oriented PE melt (139 °C) is isothermally (128 °C) crystallized while 2D SAXS (*top*) and 2D WAXS (*bottom*) are recorded. Orientation direction is indicated by *double-headed arrows*. **a** After 68 s a highly oriented SAXS long period of 110 nm (*diamond-headed arrow*) is observed, whereas the WAXS shows only an amorphous halo. **b** After 145 s, 3 weak and isotropic WAXS reflections (*open arrow heads*) are observed, whereas a highly oriented SAXS long period has grown. *Arrows with filled heads* indicate the room temperature positions of the respective reflections. **c** After 20 min of crystallization and quenching, WAXS shows the full set of isotropic PE reflections, whereas SAXS data show low long-period and complex orientation

different experiments [22, 23]. It appears noteworthy that some transient orientation of the WAXS reflections was found [23] in the period between 3 and 5 min after quenching. During this period lamellar thickening has been observed in the SAXS. Thereafter the crowding of the remnant volume with imperfect crystallites has been found to completely erase the WAXS orientation, again.

Slices through the SAXS patterns as a function of crystallization time

The quantitative evolution of the SAXS in the meridional direction is demonstrated by curves sliced along the meridian. Figure 3 shows the development for the experiment carried out at the lower crystallization temperature of 124 °C. Every 10th extracted curve is shown. Obviously the change during the first 50 s and after 150 s is low compared to the variation in between. On the linear intensity scale the type of scattering appears to be diffuse, whereas on the logarithmic scale (Fig. 1e) faint correlations among lamellar domains are present.

Although the respective slices from the crystallization experiment carried out at 128 °C (Fig. 4) exhibit a developing long-period maximum and thus a higher amount

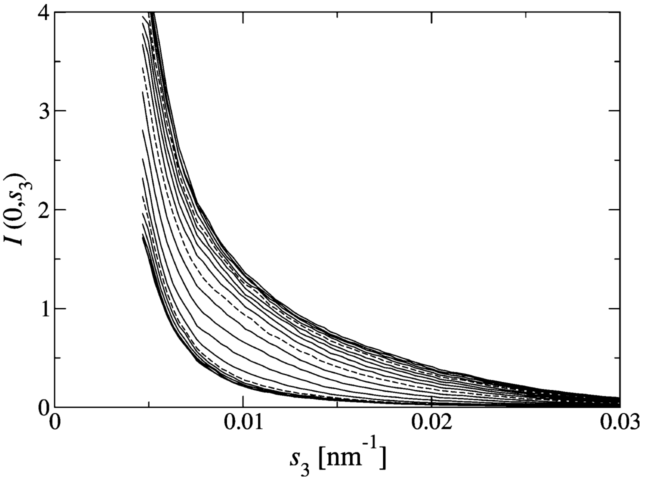

Fig. 3 PE crystallization at 124 °C. Growth of the meridional SAXS, $I(s_{12}{=}0,s_3)$ in steps of 10 s after quenching from 139 °C. *Dashed curves* mark the states after 50, 100, and 150 s

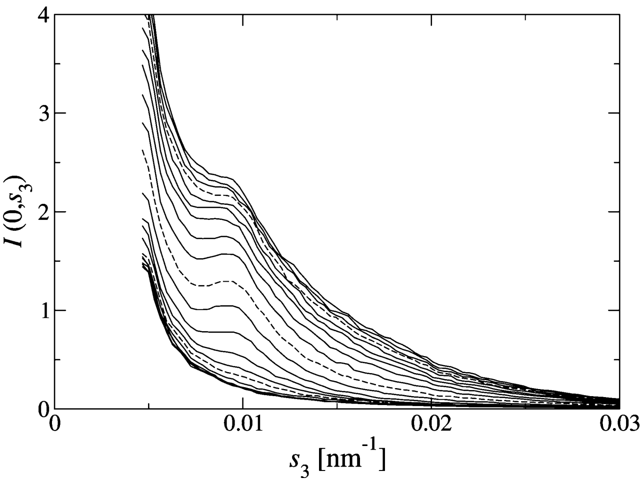

Fig. 4 PE crystallization at 128 °C. Growth of the meridional SAXS, $I(s_{12}=0,s_3)$ in steps of 10 s after quenching from 139 °C. *Dashed curves* mark the states after 50, 100, and 150 s

of inter-domain correlations, the principal character of nanostructure evolution is similar. Most of the variation of the SAXS in the fiber direction takes place between 50 and 150 s after quenching from the melt. The formation of crystallites, on the other hand, follows different schemes for the different experiments. This observation is a further indication that the formation of nanostructure ("nanoforming") is the primary structure formation mode in our material, whereas the formation of crystallites is a secondary mechanism.

Slices of scattering intensity are frequently presented for the purpose of nanostructure discussion even though almost 40 years ago it was reported that they are not suitable for an in-depth structure discussion of domain size and arrangement in a chosen direction of the sample. Instead, intensity projections should be studied [15, 43, 44]. Let us consider one of the most important cases. For the information on domain size and arrangement in the fiber direction we have to consider the projection

$$\{I\}_1(s_3) = 2\pi \int s_{12} I(s_{12}, s_3) ds_{12}$$

The structure information of $\{I\}_1(s_3)$ has been named the *longitudinal structure* by Bonart [43]. Without application of any model $\{I\}_1(s_3)$ is Fourier-transformed into Vonk's one-dimensional correlation function [45, 46], the 2nd derivative of which is Ruland's interface distribution function (IDF) [41] $g1(r_3)$. With respect to the multidimensional chord distribution function (CDF), $z(\mathbf{r})$, the longitudinal structure is $g_1(r_3)=z(0,r_3)$—the *slice in real space* of the CDF along the meridian. While $I(\mathbf{s})$ and the correlation function present a distorted [18, 47] view on the polydispersity of nanodomains and their mutual correlations, IDF and CDF are directly built from the undistorted [18] number distributions [41] of the domain sizes.

SAXS chord distribution functions

A real-space representation of the complete anisotropic nanostructure information contained in the SAXS patterns is the CDF $z(\mathbf{r})=z(r_{12},r_3)$. Figure 5 shows a sequence of CDFs from the experiment in which isothermal crystallization was performed at 128 °C. Figure 5e shows the CDF of the un-molten PE rod for reference. The triangular peaks are proportional to the total surface of contact between the layer structure and its imagined displaced ghost as a function of displacement, $\mathbf{r}$. Thus the extension of the triangles in lateral direction (r_{12}) is twice the layer extension. The sharpness of the triangles in the meridional direction shows that the thickness of the layers is rather uniform. The light line indicated on the surface that is running along the meridian marks the IDF curve [41] of the longitudinal structure [43] in the fiber. Its quantitative variation will be discussed in following sub-sections.

Figure 5b displays the nanostructure information of the melt. As published in earlier work [23] this pyramid-shaped CDF is typical for a well-molten material. Figure 5c shows the typical anisotropic nanostructure between melt and lamella formation that has already been described in the earlier paper, as well. We named it a "sofa-cushion" structure and discussed it in terms of a model of low-density regions full of entanglements (strands). The well-known semicrystalline layer system is growing from this structure. Figure 5d shows the very beginning of lamellar growth (first peak of triangular shape). More perfect lamellae are grown in the sequel (Fig. 5e,f), but the layer thickness distributions are generally wider than those in the original material.

Again we find the same states of nanostructure development in the data of this study, but confirmation is not the aim of this new investigation. Instead, we exploit the high time-resolution of our new data to gain some deeper understanding of the mechanisms of nanostructure formation and crystallization in our material. Before we continue to do so, let us look at typical states of nanostructure evolution for the second crystallization experiment carried out isothermally at 124 °C. Figure 6 shows the corresponding CDFs. We remember that for this experiment WAXS, crystallization is observed as early as 32 s after quenching when the SAXS has not yet changed from the molten state. The reason for this peculiar finding is now readily established in the CDF: we observe the CDF of a system of uncorrelated layers of inhomogeneous thickness (Fig. 6b) from the beginning of our experiment instead of the CDF of a proper melt. We bear in mind that this nanostructure of remnant proto-lamellae does not show WAXS reflections. Nevertheless, the proto-lamellar structure appears to initiate early crystallization. WAXS reflections can be observed as early as 32 s (Fig. 6d and Fig. 1c)

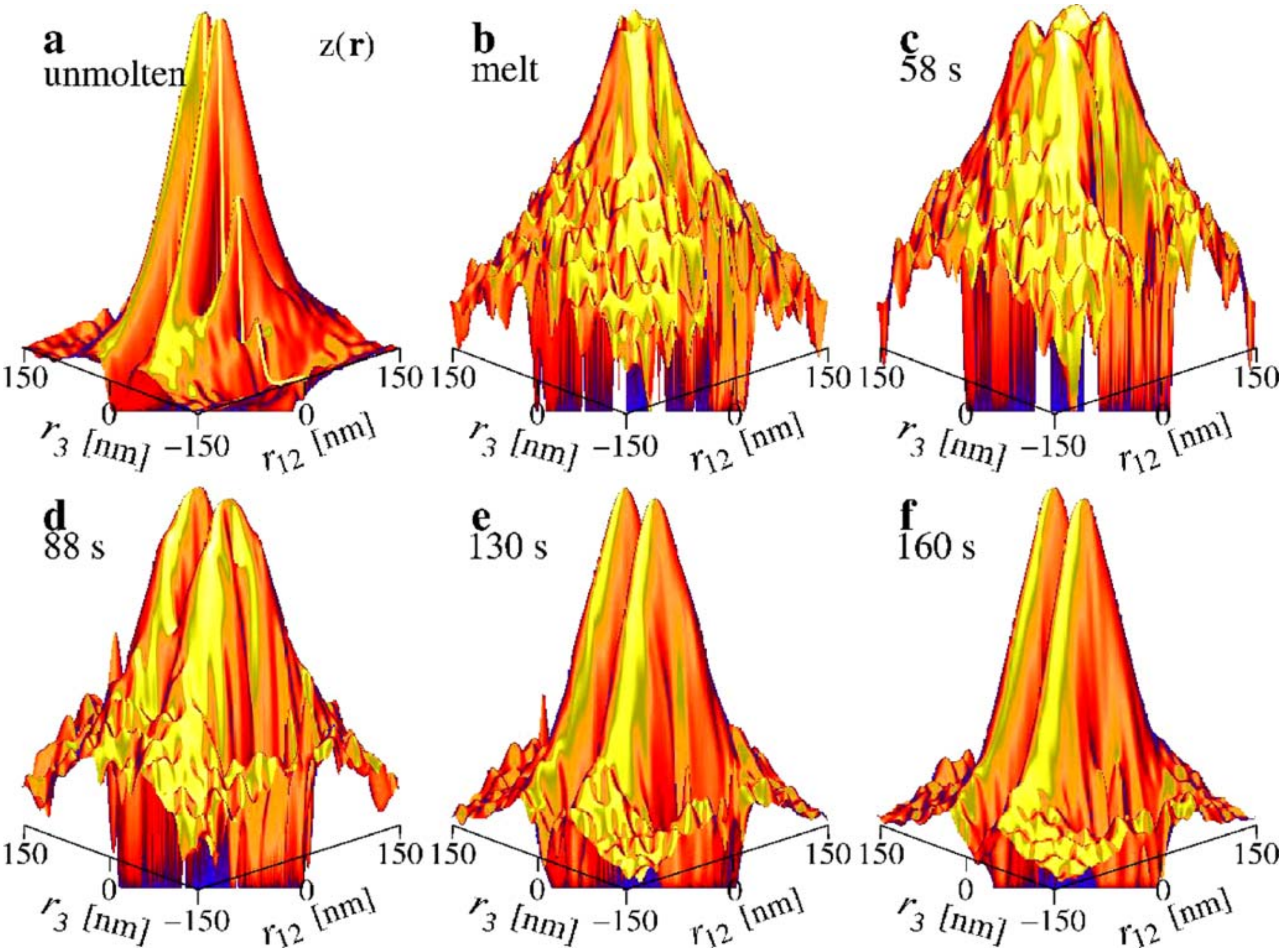

Fig. 5 Multidimensional CDFs displaying the nanostructure evolution during the early stages of anisotropic crystallization of a PE rod (isothermally crystallized from the melt at 128 °C). "Intensities" are on a logarithmic scale. **a** The un-molten material is shown for reference. The indicated *light line* along the meridian is Ruland's interface distribution function (IDF) of the longitudinal structure. **b** The melt at 139 °C just before quenching. **c** Nanostructure without crystallites 58 s after quenching at 128 °C. **d** Growing of stable layers just at the time when first crystal reflections are observed. **e**, **f** Triangular CDF peaks of well-expressed lamellae

after at a sample temperature of 135 °C. On the other hand, the expression of well-defined semicrystalline layers (Fig. 6e,f) is not coupled to this early formation of crystallites and starts many time-frames later.

Here we already benefit from the increased time resolution that no longer integrates structural variations over an exposure time of 3 s, delivering one pair of scattering patterns every 7 s [23]. The interaction between the formation of crystallites and nanostructure now appears sufficiently resolved (at a time resolution of 1 s using an integration time of 0.1 s).

Longitudinal structure during crystallization

We return to the longitudinal structure for a quantitative description of structural evolution during the early stages of isothermal crystallization. With respect to the real-space CDF the longitudinal structure is the slice $g_1(r_3)=z(0,r_3)$ in the meridional direction, i.e., Ruland's interface distribution function (IDF). For the purpose of presentation on paper the IDF has the advantage that variation of a curve is easily demonstrated and that evolution of domain stacking is readily demonstrated. Nevertheless, information on varying anisotropy is hidden. If we study the variation of these curves on a time-grid of 1 s, we expect to benefit from the high time resolution and the low exposure time of the experiment, again. Here the basic question of interest is related to the discrimination of structure fluctuation from the onset of structure evolution.

Ultimate structure

Before we start to discuss the very early structure evolution in our material during isothermal crystallization, let us first demonstrate the ultimate structure of the material before and after heat treatment in view of the IDF. Figure 7 displays the statically measured IDFs of the longitudinal structure at room temperature. Obviously all the static IDFs

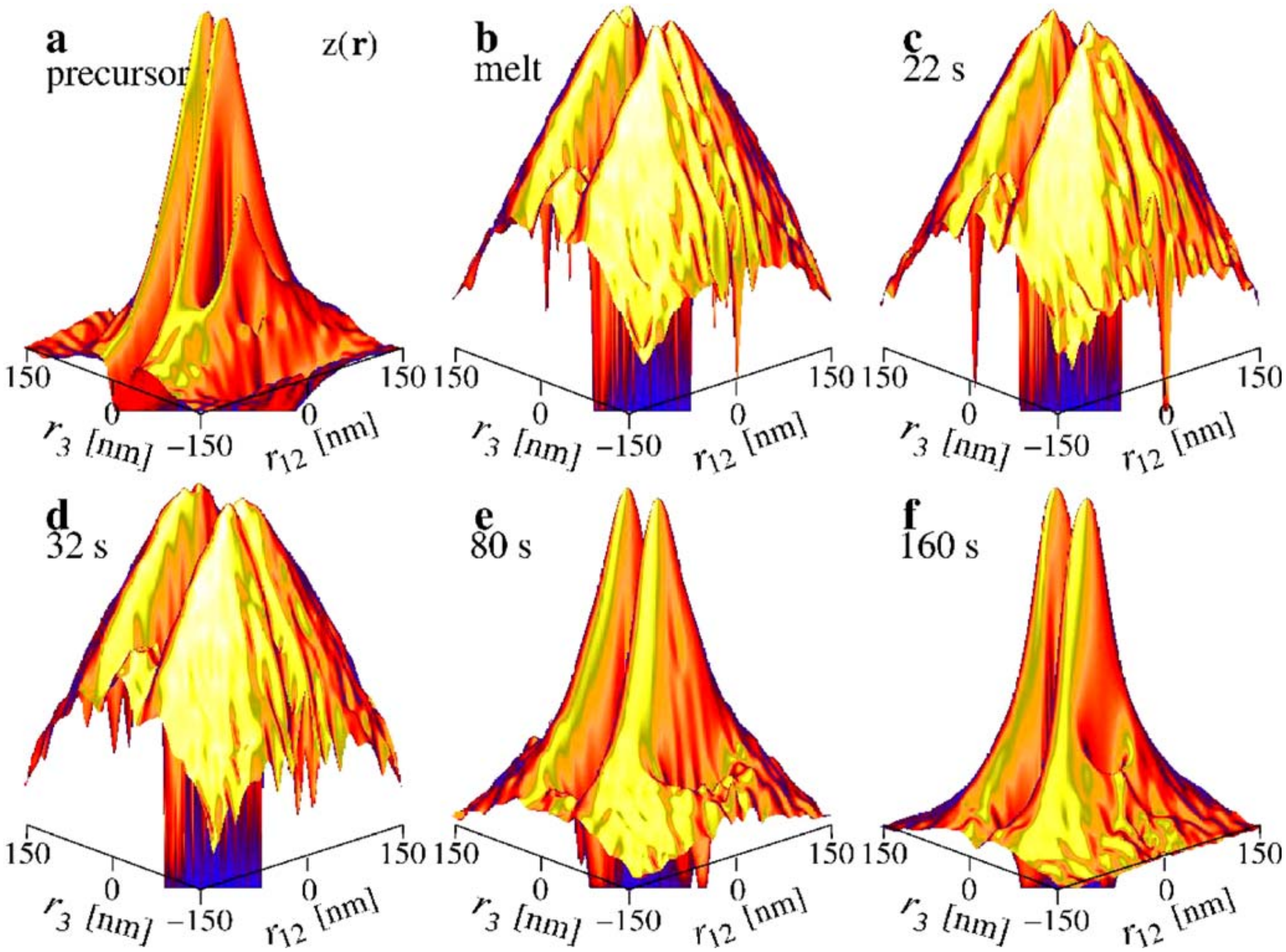

Fig. 6 Multidimensional CDFs from the crystallization experiment at 124 °C. “Intensities” are on a logarithmic scale. **a** The un-molten PE. **b** The melt at 139 °C before quenching. The CDF shows remnant proto-lamellae. **c** Proto-lamellae without crystallites 22 s after quenching at 137 °C. **d** Proto-lamellae at a stage where first WAXS crystallinity is observed 32 s after quenching now at 135 °C. **e**, **f** CDF with *narrow triangular peaks* of semicrystalline lamellae

fulfil the condition $z(0,r_3=0)\approx 0$ that should hold for a sufficiently ideal multiphase system. We have not forced fulfillment by iterative spatial frequency filtering (cf. “Experimental” part). Moreover, the point-shaped long-period reflection in the scattering intensity of the original material (Fig. 1a, 122 nm) does not play any role in the CDF and the IDF (Fig. 7, solid line): the IDFs are almost completely attenuated at structure-ghost displacements 70 nm. In the scattering patterns the low-angle peak is strong, though, because of the uneven weighting of domain thicknesses and long periods in any scattering pattern [18, 47], whereas in the CDF and the IDF, polydisperse domain statistics are represented by their number distribution [18]. Thus the volume-average long period of the original PE rod is ≈25 nm, i.e., close to the minimum of the curve (Fig. 7, solid line).

After both kinds of heat treatment the shapes of the IDFs are identical (Fig. 7, dotted and dashed lines). This repeated observation confirms the published fact that after quiescent crystallization the observed ultimate nanostructure of this

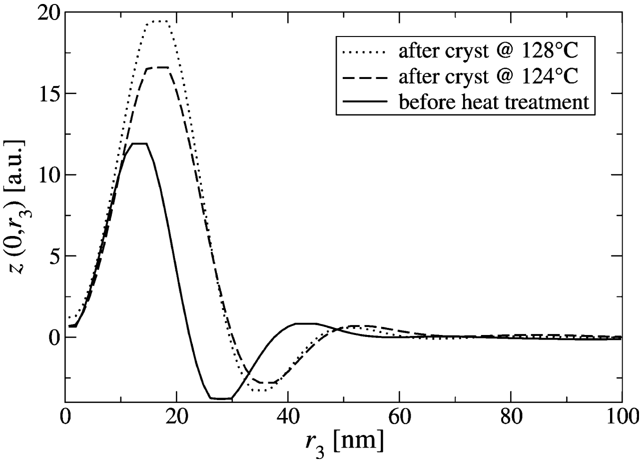

Fig. 7 Ultimate layer structure in the IDF $z(0,r_3)$ of the oriented PE material at room temperature. The *dotted curve* is scaled down by a factor of ≈0.35 with respect to the others

material is, to a first approximation, not a function of the processing under quiescent conditions [21, 23], because it is ultimately dominated by a crowd of *arranged* small crystallites that are formed late during quenching. They occupy the last free places in the *centers* of remnant amorphous regions.

The first minute after quenching

Our intention for this new study was the investigation of early structure evolution mechanisms at the beginning of isothermal crystallization. Let us start with the experiment in which the melt is nearly perfect. It probes isothermal crystallization at high temperature (128 °C). Figure 8 shows the first 40 longitudinal IDFs that cover a time of 40 s after the beginning of quenching. Groups of 10 IDFs are displayed using the same curve style. On the time-grid of 1 s we do not observe nanostructure evolution, but fluctuation of the IDF for the whole period displayed. Nevertheless, a principal structuring element is observed. There is a common peak at 20 nm. Obviously the melt exhibits a certain preference to generate proto-domains of nearly homogeneous density which measure 20 nm in the fiber direction. Beyond that distance there is not simply background, but more or less regular density oscillation (the ominous orientation-memory preserving "row structure" in our earlier study [23]) with fluctuating phase. It appears inappropriate to discuss these IDFs in terms of nanostructure or spinodal decomposition, because the observed oscillation exhibits considerable random phase shift as now it is recorded with a short cycle time and short exposure. The experiment shows that we are unable to find an early and fast mechanism of structure formation in our SAXS data. For future crystallization experiments by static X-ray scattering methods there should be little reason to further decrease the cycle time.

Figure 9 presents the respective data from the beginning of the crystallization experiment at 124 °C. Again, during this period there is no systematic structure evolution. Nevertheless, because of the fact that the nanostructured layers have not completely vanished the IDF is not fluctuating about an equilibrium melt, but about the remnant structure of uncorrelated layers of very inhomogeneous thickness. The most probable layers show a thickness of 30 nm (maximum of the curves), and the layer thickness distribution extends up to 100 nm. WAXS reflections are already showing up during the period documented in this plot. It appears noteworthy that no change of the nanostructure or its dynamics indicates the onset of WAXS crystallization.

From nanostructure fluctuation to nanostructure evolution

Although early nanostructure evolution mechanisms cannot be resolved in our new experiments, we now can study with high time resolution the interval of time in which crystallization is starting. Figure 10 shows the evolution of the longitudinal IDF in the high-temperature crystallization experiment. In the 10 s before we observe WAXS reflections the IDF keeps fluctuating (dotted curves) but the background is no longer the zero level. Instead, it resembles the structure of uncorrelated layers of inhomogeneous thickness from Fig. 9. The first 3 dashed curves (82, 84, and 86 s) still show a slowly increasing crowd of inhomogeneous lamellae, whereas the last 2 of the dashed curves (after 88 s) can already be attributed to the next period, during which the volume is rapidly crowded by thinner lamellae of increasing homogeneity. In this experiment we find a clear correlation between the evolution of nanosize layers with "fixed" thickness and the formation of crystallites, which can be observed in the WAXS after 85 s.

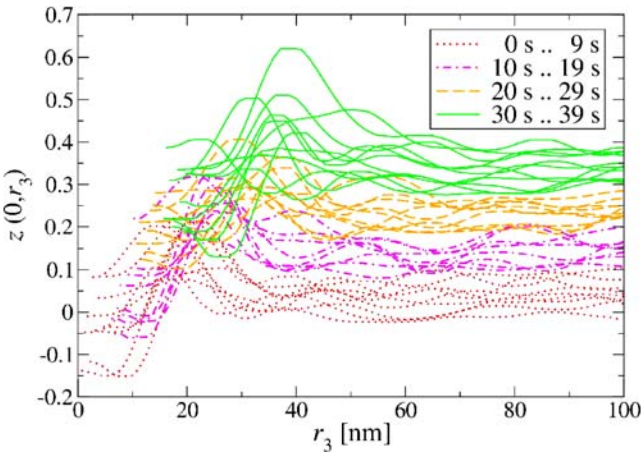

Fig. 8 Isothermal crystallization at 128 °C. Development of the IDF $z(0,r_3)$ of the oriented PE as a function of time in steps of 1 s after quenching. Curves are shifted for clarity

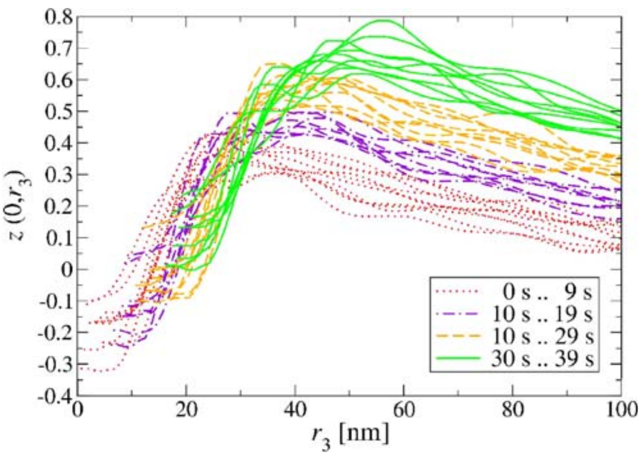

Fig. 9 Isothermal crystallization at 124 °C. Development of the IDF $z(0,r_3)$ of the oriented PE as a function of time in steps of 1 s after quenching. Curves are shifted for clarity

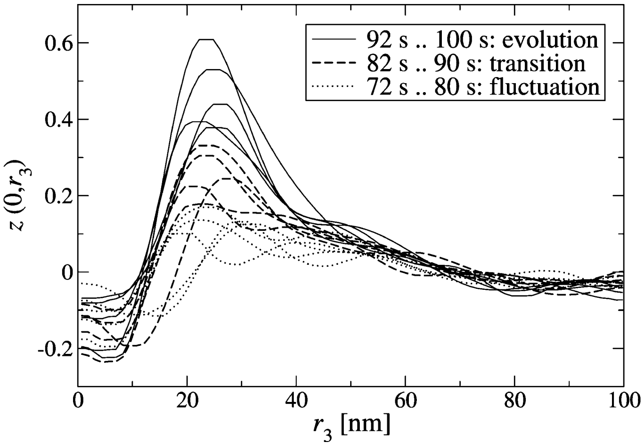

Fig. 10 Isothermal crystallization at 128 °C. Growth of the IDF $z(0, r_3)$ of the oriented PE in the time-window where first WAXS reflections are observed. *Dotted curves* before WAXS (fixed number of fluctuating lamellae), *dashed curves* as first WAXS reflections show up, *solid curves* crowding (increasing number of stable lamellae)

On the other hand, there are no WAXS reflections before the material starts to form inhomogeneous proto-domains.

It appears noteworthy that the early development of a sharp long-period reflection (Fig. 4) is neither correlated with the starting of crystallization nor with the evolution of nanosize layers in CDF or IDF. The fact that the corresponding long-period peak in the CDF is faint and only detectable after logarithmic scaling, shows that the sharp SAXS reflection is generated from only a small fraction of arranged and highly oriented lamellae in the material.

For the crystallization at 124 °C the onset of nanostructure evolution is demonstrated in Fig. 11.

Even during the period in which the first WAXS reflections are observed (dotted curves) the ensemble of inhomogeneous nanosize proto-lamellae does not change. Beginning with a time 50 s after quenching (dashed curves) the proto-lamellar system starts building up (129.5 °C). Narrowing of the lamellar thicknesses and fast volume crowding starts 56 s after quenching at a temperature of 126.2 °C.

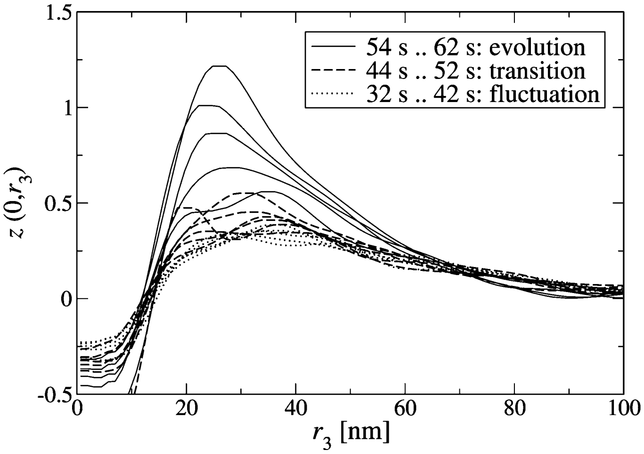

Fig. 11 Isothermal crystallization at 124 °C. Growth of the IDF $z(0, r_3)$ of the oriented PE in the time-window between nanostructure fluctuation and nanostructure evolution. WAXS crystallinity is continuously present

In summary, the evolution of nanosize domains in our studied material is not induced by crystallization. Reciprocally, the presence of nanosize proto-domains appears to be a prerequisite for crystallization. In our previous study [23] we associated these proto-domains with an early phase separation into two kinds of regions discriminated by high and low chain-entanglement density, respectively. Because of the low-time-resolution experiment we were unable to quantify their evolution. Our new data indicate that the proto-domains are not only a transient precursor of crystallization, but an important nanostructural feature that may even survive the melting of the crystallites.

Evolution during the first 3 min

Figure 12 presents the evolution of the longitudinal IDF recorded dynamically for the crystallization at 124 °C. During the primary crystallization documented here the "intensity" is rapidly increasing. Dashed curves indicate the states after 50, 100, and 150 s. After a strong domain peak there are hardly any further oscillations that would be indicative of interlamellar correlations. Thus, as already published elsewhere [19–21], the arrangement of the layers in the material appears to be predominantly random during primary crystallization. Again, the peak maximum position results in an average layer thickness of 24 nm [23].

As the material is crystallized at high temperature (128 °C) a similar chronological sequence of longitudinal IDFs is observed. Figure 13 reports the corresponding nanostructure evolution. A lower "intensity" of the IDF indicates that at the

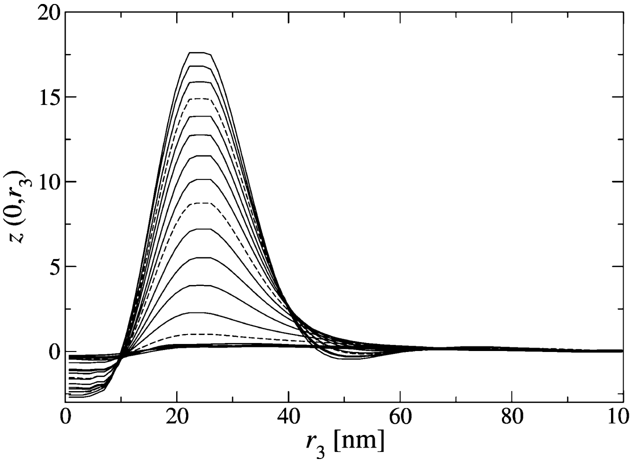

Fig. 12 Isothermal crystallization at 124 °C. Growth of the IDF $z(0, r_3)$ of the oriented PE as a function of time in steps of 10 s after quenching. *Dashed curves* show the states after 50, 100, and 150 s

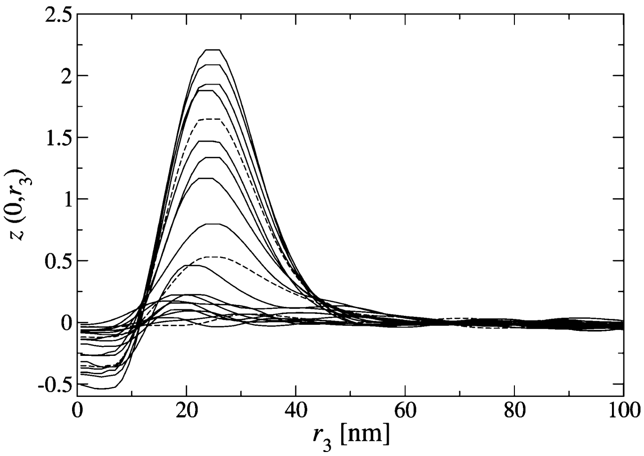

Fig. 13 Isothermal crystallization at 128 °C. Growth of the IDF $z(0, r_3)$ of the oriented PE as a function of time in steps of 10 s after quenching. *Dashed curves* show the states after 50, 100, and 150 s

higher temperature level much less lamellae are present in the irradiated volume than at the lower temperature. Nevertheless, as a function of increasing crystallization time the number of existing lamellae is increasing, as well. Interlamellar correlations are negligible. Here the placement of the layers is completely random. Thus the mechanism observed here is the ideal case of Rényi's *random car-parking process* [48–51] that has been observed during polymer crystallization several times before [19–21, 52, 53].

Model mechanisms for the quiescent isothermal crystallization

Based on our new in situ high-time-resolution scattering data we now can propose an extended model for the evolution of the semicrystalline state from the melt in our material. Proto-domains with thicknesses ranging between 20 and 100 nm are first generated by phase separation into more and less entangled regions, respectively. We cannot exclude that these proto-domains are vagrant. Thus observed SAXS of uncorrelated layers (Fig. 1b) would be compatible with a dynamic nanostructure. Crystallization can only proceed inside the disentangled proto-domains of this nanostructure. In any case, by incorporating a crystallite, a nomad proto-domain pays for settling down. During quenching from the melt there is a period in which the number of proto-domains is slowly increasing. In principle this crowding of the volume by possible nomads is not coupled to crystallization. On the other hand, when the narrowing of the domain thickness distribution sets in and the crowding of the sample volume with domains is accelerated, this process is accompanied by crystallization. Sharing of volume among vagrant domains has definitively stopped as this period and settlement has started. It appears not really surprising that, initially, the crystallites formed within the same proto-domain do not share the orientation of the layer. Moreover, because the settlement is continued during the quiescent isothermal experiment there is always a majority of unoriented newcomers, even if the older settlers use their opportunity to re-crystallize in order to match the orientation of the crystallites to the layer orientation. In our earlier study [23] we observed such a tendency during a period between 3 and 5 min after starting the quiescent isothermal crystallization. As reported earlier as well, the late settlers take the small leftovers. Because they are not the children of extended proto-lamellae any more, they exhibit not even a tendency for preferential orientation on a higher level. Instead, they prefer to keep equal distance from their next neighbors (i.e., no random placement but insertion [54, 55]) and thus imprint the ultimate long period of the material.

Conclusions

Because of the fact that we are studying the crystallization in highly anisotropic specimens with 2D detectors, we are able to observe the evolution of oriented nanostructure and of crystallites directly. By means of the CDF method we visualize and discuss structure evolution without a need for a priori modeling.

In contrast to the classical approach to structure evolution we are not focusing on a fundamental confirmation of classical notions by means of approximative laws with its inherent limitation concerning the choice of suitable sample materials. Our interest is the scanning of structure evaluation in technical materials with as little modeling background as possible. As the collection of results grows, we should become able to detect some rules of thumb that may help to practically improve the properties of polymer materials.

If we dare to extrapolate from the narrow basis of data that we have collected so far, in the initial period of the nanostructure evolution inside our PE material there is obviously no strict coupling between SAXS and WAXS, i.e., between nanostructure formation and crystallization. A similar result has recently been obtained by us in a crystallization study of ultra-high molecular weight polyethylene [53]. The presented high-time-resolution data now clearly demonstrate that there may be nanostructure (proto-domains) without crystallinity. Moreover, in the studied quiescent process the orientation of even the very first crystallites is not coupled to the orientation of the first proto-lamellae. Reciprocally, coupling of chain direction to the normal of lamellae appears to be a result of ripening—according to indications in our earlier study [23]. Thus our observations do not support the ideal notion of nucleation-and-growth [4, 8, 13]. They are more compatible with the model of a spinodal decomposition [1, 5, 12] at least what a phase separation before crystallization is concerned. The coincidence of isotropic WAXS and anisotropic SAXS is a strong indication for Strobl's mechanism of lamella formation from blocks [56].

If the observed mechanisms would generally describe the quiescent oriented crystallization of polyethylene, a chance to control the ultimate structure of the material should focus on 5 points: (1) choose an appropriate molecular weight distribution for the purpose of entanglement control, (2) force a regular arrangement of the proto-domains, (3) orient the chain segments in the proto-domains, 4 convert them fast and simultaneously into settled domains, (5) suppress formation of latecomers. Most probably even a subset of these points cannot be controlled under quiescent processing conditions: in this case the practical value of quiescent crystallization studies were limited.

Acknowledgments We acknowledge the support of Dipl. Ing. F. Tschöpe concerning the high-pressure injection-molding and the European Synchrotron Radiation Facility (ESRF), Grenoble, France for provision of the synchrotron radiation facilities at beamline ID02 in the frame of project SC-1679. Financial support of this study by the Deutsche Forschungsgemeinschaft (DFG STR501/4-1) is gratefully acknowledged.

References

1. Wang W, Ruland W, Cohen Y (1993) Acta Polym 44:273
2. Allegra G, Meille SV (1999) Phys Chem Chem Phys 1:5179
3. Heck B, Hugel T, Iijima M, Sadiku E, Strobl G (1999) New J Phys 1:17.1
4. Wang ZG, Hsiao BS, Sirota EB, Srinivas S (2000) Polymer 41:8825
5. Dreezen G, Ivanov DA, Nysten B, Groeninckx G (2000) Polymer 41:1395
6. Heck B, Hugel T, Iijima M, Strobl G (2000) Polymer 41:8839
7. Somani RH, Yang L, Hsiao BS, Agarwal PK, Fruitwala HA, Tsou AH (2002) Macromolecules 35:9096
8. Heeley EL, Maidens AV, Olmsted PD, Bras W, Dolbnya IP, Fairclough JPA, Terrill NJ, Ryan AJ (2003) Macromolecules 36:3656
9. Bras W, Dolbnya I, Detollenaere D, van Tol R, Malfois M, Greaves G, Ryan A, Heeley E (2003) J Appl Cryst 36:791
10. Somani RH, Yang L, Hsiao BH, Fruitwala H (2003) J Macromol Sci Part B Phys B42:515
11. Yamazaki S, Hikosaka M, Toda A, Wataoka I, Yamada K, Tagashira K (2003) J Macromol Sci Part B Physics B42:499
12. Ania F, Flores A, Baltá Calleja FJ (2003) J Macromol Sci Part B Phys 42:653
13. Panine P, Urban V, Bösecke P, Narayanan T (2003) J Appl Cryst 36:991
14. Stribeck N (1993) Colloid Polym Sci 271:1007
15. Stribeck N (2000) ACS Symp Ser 739:41
16. Stribeck N (2001) J Appl Cryst 34:496
17. Stribeck N (2002) Colloid Polym Sci 280:254
18. Stribeck N (2006) J Appl Cryst 39:237
19. Stribeck N, Almendarez Camarillo A, Cunis S, Bayer RK, Gehrke R (2004) Macromol Chem Phys 205:1445
20. Stribeck N (2004) Macromol Chem Phys 205:1455
21. Stribeck N, Almendarez Camarillo A, Bayer R (2004) Macromol Chem Phys 205:1463
22. Stribeck N, Bayer R, Bösecke P, Almendarez Camarillo A (2005) Polymer 46:2579
23. Stribeck N, Bösecke P, Bayer R, Almendarez Camarillo A (2005) Progr Coll Polym Sci 130:127
24. Ania F, Rueda DR, Calleja FJB, Krosigk GV (2000) J Mater Sci 35:5199
25. Stribeck N, Bayer R, von Krosigk G, Gehrke R (2002) Polymer 43:3779
26. Narayanan T, Diat O, Bösecke P (2001) Nucl Instrum Methods Phys Res Sect A 467–468:1005
27. Bösecke P, Diat O (1997) J Appl Cryst 30:867
28. Urban V, Panine P, Ponchut C, Bösecke P, Narayanan T (2001) J Appl Cryst 36:809
29. VNI, pv-wave manuals. V 7.5 (2001), Boulder, Colorado
30. Stribeck N, Web Page. http://www.chemie.uni-hamburg.de/tmc/stribeck/
31. Buhmann MD (2000) Acta Numerica 9:1
32. Stribeck N (2003) Anal Bioanal Chem 376:608
33. Stribeck N, Buzdugan E, Ghioca P, Serban S, Gehrke R (2002) Macromol Chem Phys 203:636
34. Stribeck N (2003) Fibr Text EE 11:33
35. Stribeck N, Androsch R, Funari SS (2003) Macromol Chem Phys 204:1202
36. Stribeck N, Fakirov S, Apostolov AA, Denchev Z, Gehrke R (2003) Macromol Chem Phys 204:1000
37. Stribeck N, Funari SS (2003) J Polym Sci Part B Polym Phys 41:1947
38. Stribeck N, Almendarez Camarillo A, Nöchel U, Schroer C, Kuhlmann M, Roth SV, Gehrke R, Bayer RK (2006) Macromol Chem Phys 207:1239
39. Stribeck N, Fakirov S (2001) Macromolecules 34:7758
40. Vonk CG (1979) Colloid Polym Sci 257:1021
41. Ruland W (1977) Colloid Polym Sci 255:417
42. Ruland W (1978) Colloid Polym Sci 256:932
43. Bonart R (1966) Kolloid Z u Z Polymere 211:14
44. Fischer EW (1969) Colloid Polym Sci 231:458
45. Vonk CG, Kortleve G (1967) Colloid Polym Sci 220:19
46. Strobl GR, Schneider M (1980) J Polym Sci Part B Polym Phys B18:1343
47. Schmidt PW, Brill LO (1967) In: Rowell RR, Stein RS (eds), Electromagnetic scattering. Proceedings of ICES 2, Amherst, MA, June 1965, pp 169–186, Gordon & Breach, New York
48. Rényi A (1958) Publ Math Inst Budapest 3:109
49. Rényi A (1963) Sel Transl Math Stat Prob 4:203
50. Burgos E, Bonadeo H (1987) J Phys A 20:1193
51. Bonnier B, Boyer D, Viot P (1994) J Phys A 27:3671
52. Ghioca P, Buzdugan E, Stribeck N, Serban S, Stancu R, Cherchez I, Stinga F (1998) Mater Plast 35:82
53. Almendarez Camarillo A, Roth SV, Bösecke P, Buchner S, Krenn K, Gehrke R, Stribeck N (2006) J Mater Sci (in press)
54. Wang J, Alvarez M, Zhang W, Wu Z, Li Y, Chu B (1992) Macromolecules 25:6943
55. Hsiao BS, Gardner KH, Wu DQ, Chu B (1993) Polymer 34:3996
56. Hugel T, Strobl G, Thomann R (1999) Acta Polym 50:214